



Residual stress and deformation in wire-feed electron beam additive manufactured aluminum components

Dongqi Zhang¹ · Dong Du¹ · Shuai Xue¹ · Junjie Qi¹ · Ze Pu¹ · Yunpeng Lu² · Yingying Tang² · Baohua Chang¹

Received: 7 November 2023 / Accepted: 30 January 2024 / Published online: 12 February 2024
© The Author(s), under exclusive licence to Springer-Verlag London Ltd., part of Springer Nature 2024

Abstract

Electron beam additive manufacturing (EBAM) has broad application prospects in the preparation of large structural components such as those in aerospace structures. It is of great significance to have a deep understanding of the residual stress distribution and deformation of EBAM. A three-dimensional transient thermal–mechanical coupling model was established for the comprehensive investigation of the deformation and residual stress of aluminum alloy components prepared by wire-feed EBAM for the first time. The reliability of the simulation model was verified by comparing the predicted temperature, stress and deformation with experimentally measured values. The influence of heat input on residual stress distribution and deformation was studied using the verified model. The simulation results indicate that reducing heat input is an efficient approach to reducing deformation and residual stress. The developed model can be a powerful tool to optimize process parameters to reduce the residual stress and deformation of EBAM aluminum alloy components.

Keywords Wire-feed · Electron beam additive manufacturing · Aluminum alloy · Residual stress · Deformation

1 Introduction

Additive manufacturing (AM), as an emerging manufacturing technology, has attracted worldwide attention in the last few decades owing to its ability to quickly produce complex shaped structures [1–3]. Additive manufacturing technology usually uses powder or wire as raw materials, and parts are prepared layer by layer under the action of heat sources such as lasers, electron beams, and arcs [4–6]. Among numerous metal materials, aluminum alloy has become the second most commonly used structural alloy after steel on account of its exceptional properties and low-density characteristics, playing an important role in the aerospace industry [7, 8]. However, there are many problems with additive manufacturing aluminum alloys. For example, aluminum alloys are prone to oxidation at high temperatures [9] and are prone to generating a large number of pores [10]. The

high reflectivity of aluminum alloys to lasers leads to low energy utilization [11].

The additive manufacturing technology using an electron beam as a heat source can effectively solve the above-mentioned problems in aluminum alloy processing. There are two technologies: electron beam selective melting (EBSM) technology using powder as raw material [11, 12] and wire-feed electron beam additive manufacturing (EBAM) technology using wire as raw material [13, 14]. The EBAM technology using wire as raw material has the advantages of large forming size and high efficiency, which is suitable for manufacturing large structural components such as those in aerospace structures and has attracted the attention of researchers in recent years [15–17].

However, repeated thermal cycles and large temperature gradients during additive manufacturing can lead to very high residual stress [18], which is detrimental and may restrict the widespread application of metal additive manufacturing in industry. Compared to additive manufacturing technology using laser and arc as heat sources, additive manufacturing technology using the electron beam as heat source has a lower cooling rate in vacuum, which is very beneficial for controlling residual stress. There are various experimental methods for measuring residual stress, such as X-ray diffraction [19, 20], hole drilling method [21, 22], and neutron

✉ Baohua Chang
bhchang@tsinghua.edu.cn

¹ State Key Laboratory of Tribology in Advanced Equipment, Department of Mechanical Engineering, Tsinghua University, Beijing 100084, China

² Capital Aerospace Machinery Co., Ltd., Beijing 100076, China

diffraction [23, 24]. However, these experiments are both expensive and time-consuming. Therefore, the finite element method (FEM) is a prevalent approach in thermomechanical analysis to predicate residual stress and deformation.

Sun et al. [25] analyzed the residual stress distribution characteristics of aluminum alloy wire arc additive manufacturing (WAAM) components through numerical simulation. Zhao et al. [26] established a coupled finite element model for the thermal structure of selective laser melting (SLM) of 7075 aluminum alloy. An investigation was conducted to analyze how variations in process parameters influenced temperature and stress distributions. Caiazzo et al. [27] established a residual stress analysis model based on laser directed energy deposition (DED) of 2024 aluminum alloy. By comparing the actual stress with X-ray diffraction results, the correctness of predicting residual stress was verified. Vastola et al. [28] used Ti6Al4V alloy as the research object to conduct finite element modeling of electron beam selective melting process. They investigated how the magnitude and distribution of residual stress were influenced by various factors. Chen et al. [29] established a thermodynamic model considering solid-state phase change (SSPC) temperature to simulate the process of Ti6Al4V alloy component fabricated by EBAM, and proposed a method for controlling deformation. However, there are few reports on the finite element simulation of residual stress in the manufacturing of aluminum alloy with wire-feed EBAM. Therefore, it is essential to establish a thermal–mechanical coupling model for the process of aluminum alloy fabricated by wire-feed EBAM, which can be used to clarify the occurrence mechanism and control measures of residual stress in EBAM and has important guiding significance for the manufacturing of high-performance aluminum alloy aerospace structural components.

In this study, the aluminum alloy wire BJ-380D was used to construct a thin-wall structure on the 2A14 substrate by wire-feed EBAM. A thermal–mechanical coupling simulation model was established to simulate the manufacturing process of wire-feed EBAM and systematically predict the temperature, stress and deformation developed in the built aluminum alloy structure for the first time. The model's accuracy was confirmed through a comparison between the computed residual stress and measured by hole drilling and X-ray measurement methods. On this basis, the residual stress distribution in wire-feed EBAM was elucidated. Quantitative analysis was conducted on the correlation between residual stress, deformation, and heat input, providing a

guideline for controlling residual stress and deformation in the fabrication of large aluminum alloy components by wire-feed EBAM.

2 Experiment method

The substrate used in the wire-feed EBAM experiment was 2A14 aluminum alloy, and the wire material was BJ-380D aluminum alloy with a diameter of 1.6 mm. Table 1 shows the chemical compositions of BJ-380D wire and 2A14 substrate. The EBAM experiments were completed by the ZComplexX3 vacuum electron beam wire-feed additive manufacturing system. The electron beam voltage was 60 kV and the substrate movement speed was 400 mm/min. To achieve good deposition quality, the current of the first layer was set to 30 mA, the second layer was 25 mA, and the remaining layers were 20 mA. The dwell time between each layer was 60 s.

The thermocouples were used to measure the thermal cycle during the EBAM deposition process, as shown in Fig. 1. After the EBAM process, the residual stress was measured using the XRD method and hole drilling method. The Tianyuan 3D scanning system was used to perform 3D reconstruction on the specimen before and after deposition, and the point cloud data obtained was processed in CloudCompare software to create the coordinate cloud map of the specimen in the height (Z-axis) direction, based on which the deformation of the substrate after deposition was calculated.

3 Numerical modeling

3.1 Geometry model and boundary conditions

3.1.1 Geometry model

Figure 2 (a) is a schematic diagram of the geometric model. The size of the substrate was 200 mm × 200 mm × 10 mm. The dimensions of the deposited wall structure were set to be 100 mm × 7 mm × 9.8 mm based on the actual experimental results. The wall consisted of 14 layers, each with a thickness of 0.7 mm. The scanning path was in a reciprocating scanning mode along the X-axis. The software used for numerical simulation is ABAQUS, and the birth and death technique was used to simulate the forming process of the deposition layers [25, 30]. Birth and death mean the activation and deactivation

Table 1 Chemical compositions of BJ-380D wire and 2A14 substrate (wt%)

Element	Cu	Si	Mg	V	Mn	Fe	Zn	Ni	Ti	Zr	Cr	Al
BJ-380D	2.2	3.7	0.007	0.12	/	0.14	0.01	0.005	0.1	0.14	0.063	Bal
2A14	4.1	0.7	0.6	/	0.7	0.45	0.28	0.1	0.12	/	/	Bal

Fig. 1 Positions of thermocouples installed to measure temperature variations in the wire-feed EBAM process

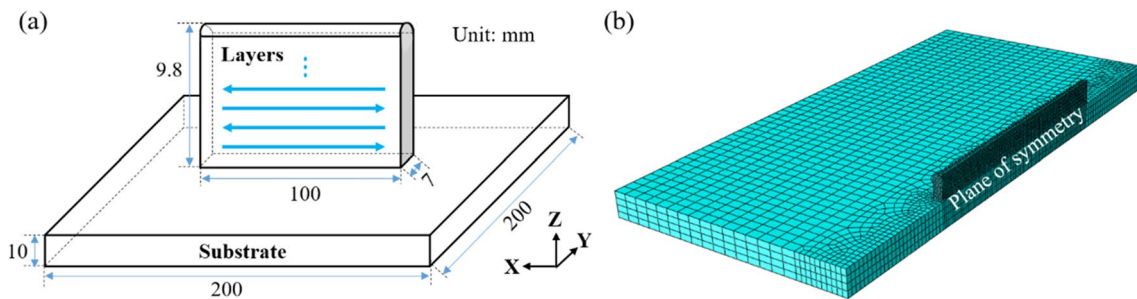
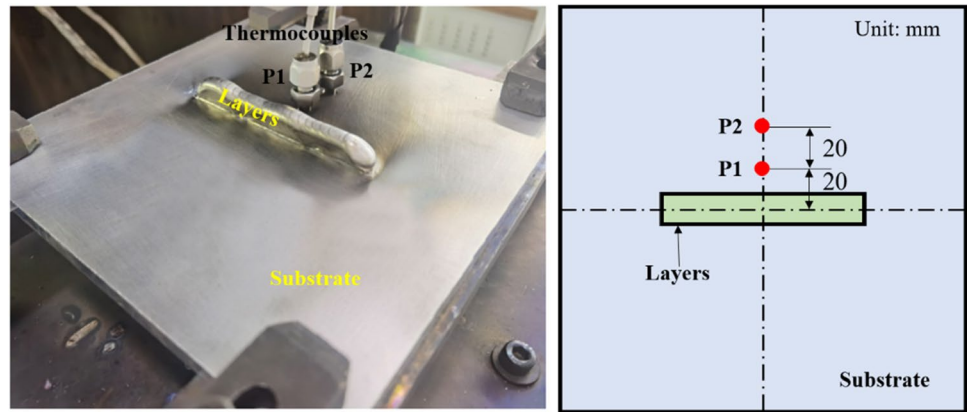


Fig. 2 **a** Schematic diagram and dimensions of the EBAM component, **b** Finite element mesh

of the elements. All pre-established elements of the deposition layers were first deactivated prior to the start of the analysis, and then corresponding elements of the deposition layers were activated step by step as the heat source moved until the deposition process was completed. The symmetry of the specimen was considered in constructing the finite element to save calculation time and cost.

On the premise of ensuring the calculation accuracy of the FE model, the overall number of grids was controlled to reduce calculation time. Due to the instantaneous heating of the electron beam, there was a significant temperature change in the deposition layer and its surrounding areas. Therefore, this model used finer grids for the deposition layer and its surrounding areas to ensure computational accuracy. At the same time, the substrate part far from the center of the heat source was calculated with a relatively coarse grid to control the overall number of grids and improve computational efficiency. The grid size of the deposition layer was 1 mm × 0.875 mm × 0.35 mm and the grid size of the substrate away from the deposition layer was 5 mm × 4 mm × 2.5 mm. The entire finite element model consisted of 19748 DC3D8 eight-node linear heat transfer hexahedral elements, as shown in Fig. 2 (b).

3.1.2 Boundary conditions

In the initial stage of the EBAM process, there is no heat input into the substrate. Therefore, the initial temperature is set to 30 °C, which is the thermal initial condition. In addition, the ambient temperature is also set to 30 °C. Due to the fact that EBAM is carried out in a vacuum environment, the thermal convection is ignored. The heat dissipation boundary conditions only include heat radiation, and the heat radiation expression is [30, 31]:

$$k \frac{\partial T}{\partial n} = -\sigma \epsilon (T^4 - T_0^4) \tag{1}$$

where σ denotes the Stefan-Boltzmann constant, ϵ is the surface emissivity.

The schematic diagram of clamping and fixing the substrate is shown in Fig. 3(a). To approach the actual situation as closely as possible, the mechanical boundary conditions in finite element calculation are set as shown in Fig. 3(b). Among them, the nodes below the fixture are set to $UX = UY = UZ = 0$, all nodes near the supports on both sides of the substrate are set to $UZ = 0$, and the nodes at the symmetry plane are set to $UY = 0$.

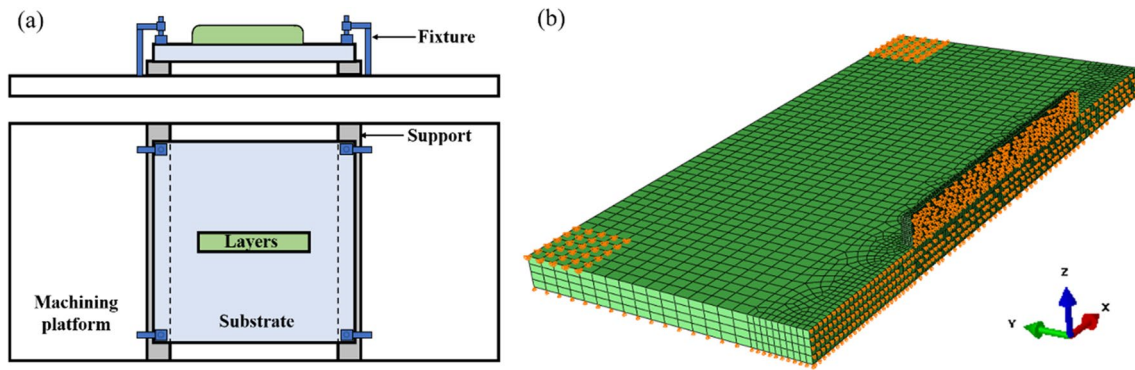


Fig. 3 **a** Schematic diagram of substrate fixed in EBAM process, **b** Boundary conditions applied in EBAM models

Table 2 Physical properties of 2A14 aluminum alloy

Temperature (°C)	Specific heat capacity (J/(kg·°C))	Thermal Conductivity (W/(m·°C))	Thermal expansion coefficient (1/°C)	Young's modulus (GPa)
50	890	134	2.20E-05	70
100	924	137	2.29E-05	69
150	943	140	2.34E-05	67.5
200	964	144	2.38E-05	66
250	987	147	2.43E-05	63.5
300	1010	150	2.47E-05	61
350	1030	154	2.49E-05	58.5
400	1060	159	2.52E-05	56
450	1090	165	2.54E-05	52.5

3.2 Material properties and heat source model

3.2.1 Material properties

The substrate used in this study is 2A14 aluminum alloy, and the wire material is BJ-380D aluminum alloy welding wire. During the electron beam heating process, the thermophysical properties of both materials will change. The calculation of temperature and stress involves many material thermophysical parameters. It is assumed that the material parameters are isotropic and the influence of latent heat is not taken into account. Due to the similarity in chemical composition of the two materials, there are few research reports on BJ-380D aluminum alloy welding wires, so the material parameters of 2A14 are used in the calculations. The density and Poisson's ratio vary little with temperature, so they are set as constants. The density of 2A14 aluminum alloy is $2.80 \times 10^3 \text{ kg/m}^3$ and the Poisson's ratio is 0.33. The variation of other thermophysical parameters of the materials with temperature was considered in this calculation, as shown in Table 2. Due to the significant differences in

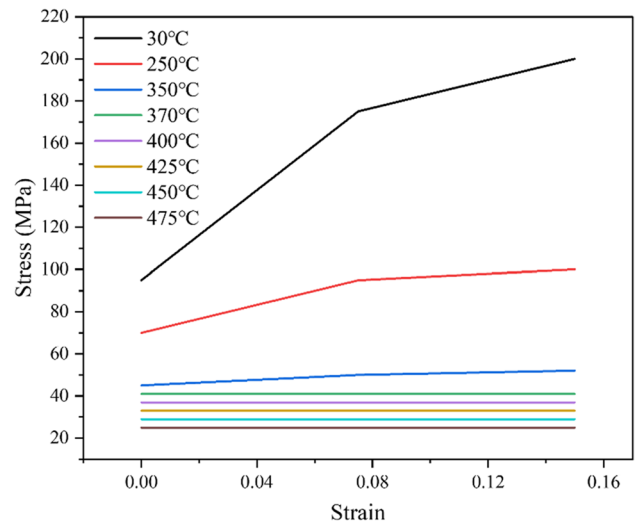


Fig. 4 Stress—plastic strain relationship at different temperatures

mechanical properties of aluminum alloys at different temperatures, this factor needs to be considered in the calculation. The stress—plastic strain relationship used in the simulation is shown in Fig. 4.

3.2.2 Heat source model

The wire-feed EBAM process employed a double-ellipsoidal heat source model and is written as [32, 33]:

$$q_1(x, y, z) = \frac{A6\sqrt{3}\eta f_1 UI}{a_1 bc \pi \sqrt{\pi}} \exp\left(-\frac{3x^2}{a_1^2} - \frac{3y^2}{b^2} - \frac{3z^2}{c^2}\right) x \geq 0 \quad (2)$$

$$q_2(x, y, z) = \frac{A6\sqrt{3}\eta f_2 UI}{a_2 bc \pi \sqrt{\pi}} \exp\left(-\frac{3x^2}{a_2^2} - \frac{3y^2}{b^2} - \frac{3z^2}{c^2}\right) x < 0 \quad (3)$$

where $f_1 + f_2 = 2$, f_1 and f_2 represent the distribution coefficients associated with the front and rear ellipsoidal heat sources respectively, a_1 , a_2 , b and c are the geometric parameters of double-ellipsoidal heat source, η is the energy absorption coefficient, A is the correction coefficient, U is the voltage, and I is the current. In this work, η is set to 1, A values for the first, second and subsequent layers are 0.5, 0.85 and 0.94, respectively.

4 Results and discussion

4.1 Experimental results and validation of numerical model

Two thermocouples were installed to measure the temperature changes as shown in Fig. 1. The two points were located 20 mm and 40 mm away from the center of the deposition

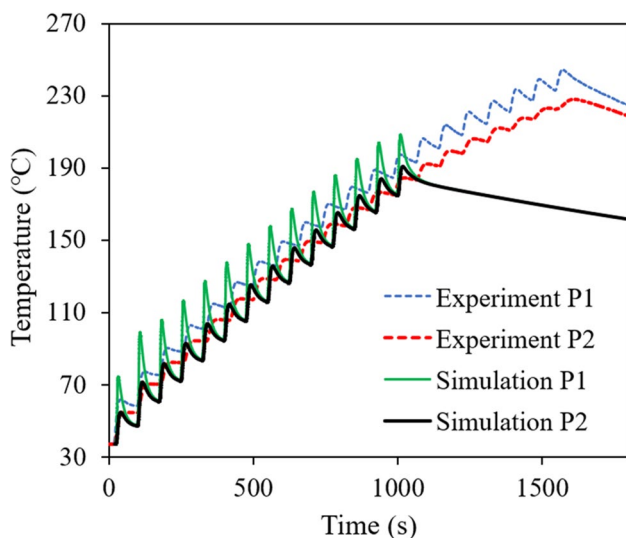


Fig. 5 Comparison of numerically predicted and experimentally measured thermal histories during deposition

layer, with a depth of 5 mm. Based on the experimentally measured temperature, the parameters of the heat source model were adjusted to ensure the accuracy of the numerical results. Figure 5 shows the temperature measurements and simulation curves at two points. It can be observed that the measured and calculated values are in good agreement. Therefore, the numerical simulation model for the EBAM process is reliable. In addition, the accuracy of the model is further ensured by comparing measured and calculated values of residual stress and deformation, which will be detailed in subsequent sections.

4.2 Temperature field distribution

Figure 6 shows the temperature distributions at different times during the EBAM process, which proceeds to the 1st, 5th, 9th, and 13th layers, respectively. The temperature contrast between the freshly deposited layer and the Ti6Al4V substrate becomes notably pronounced during the deposition of a single layer, with only a limited region of the substrate experiencing heating. As the number of deposition layers increases, more heat is transferred from the deposition layer to the substrate, and the substrate temperature gradually increases, and the size of the molten pool also significantly increases.

4.3 Residual stress distribution

Figures 7 and 8 show the longitudinal and transverse stress distributions respectively when the EBAM process proceeds to the middle of the 1st, 5th, 9th and 13th layers, the completion of deposition, and after cooling to room temperature. The simulation results indicate that due to the constraints of the clamp, there is significant stress concentration at the four corners of the substrate. The cooling and shrinkage of multiple deposited layers cause slight compressive stress on the top surface of the substrate during the deposition process.

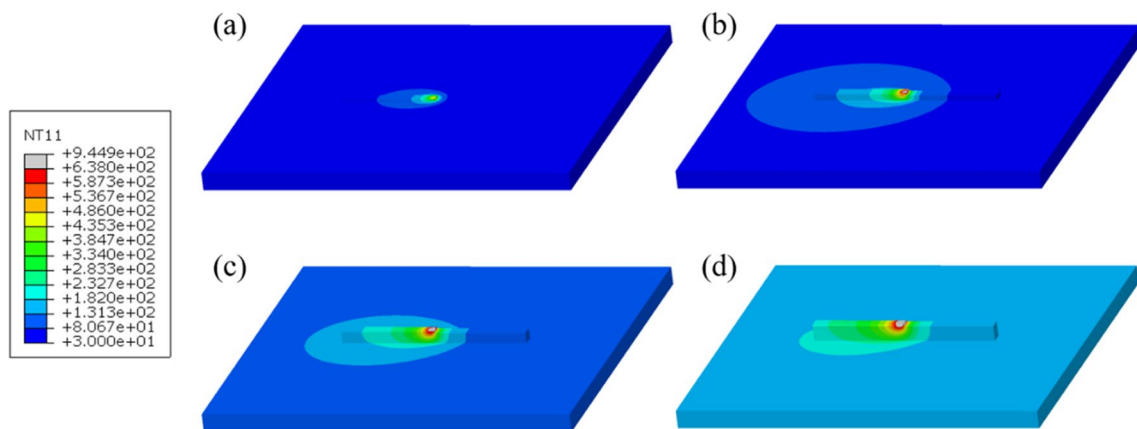


Fig. 6 Temperature distributions after (a) 1 layer, b 5 layers, c 9 layers, d 13 layers of deposition

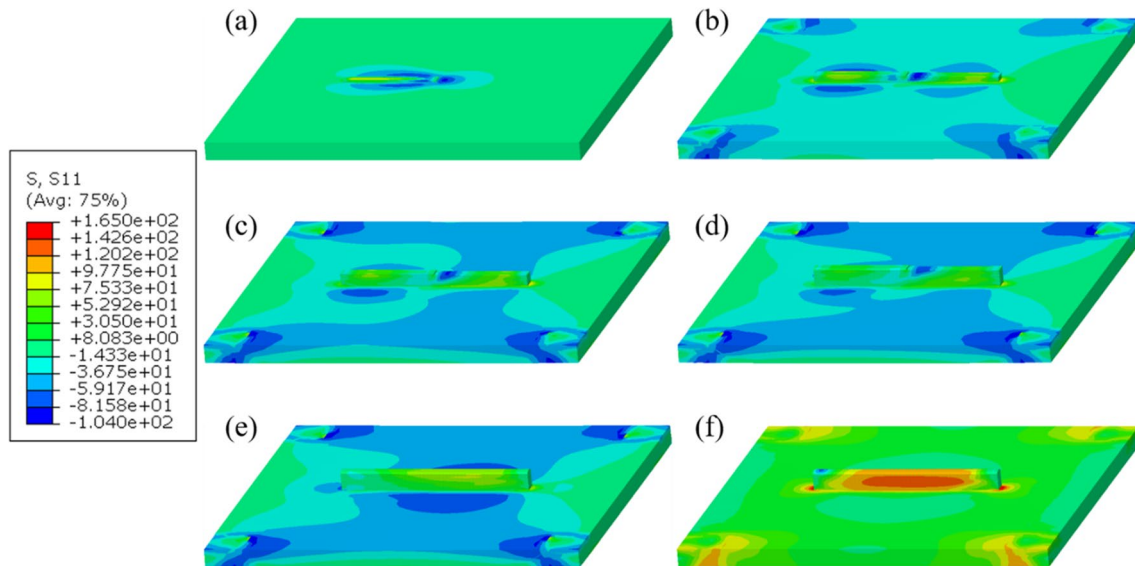


Fig. 7 Longitudinal stress distributions when EBAM process proceeds to the middle of (a) 1st layer, b 5th layer, c 9th layer, d 13th layer, to (e) completion of deposition, and (f) after cooling to room temperature

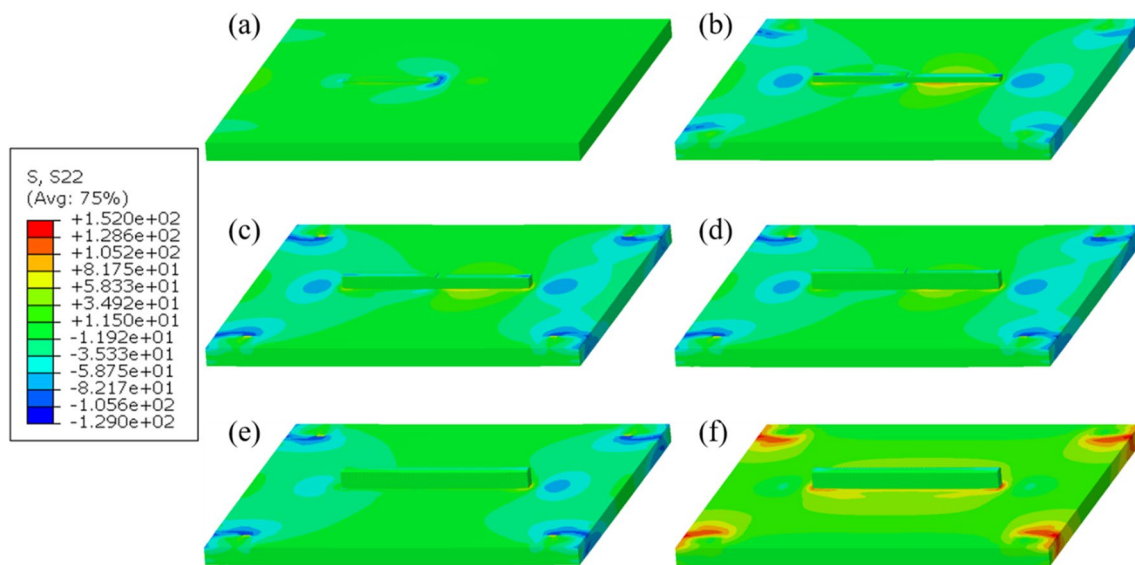


Fig. 8 Transverse stress distributions when EBAM process proceeds to the middle of (a) 1st layer, b 5th layer, c 9th layer, d 13th layer, to (e) completion of deposition, and (f) after cooling to room temperature

After cooling to room temperature, there is significant residual tensile stress at both ends of the interface between the deposition layer and the substrate. In addition, high tensile longitudinal residual stress presents in the middle part of the wall structure, while transverse stress is less significant.

After cooling to room temperature, the clamps were removed. Figure 9 shows the residual stress distribution before and after the clamp removal. It can be observed that the stress concentration around clamps disappears after removing the clamp, while the residual stress is still

concentrated in the mid-part of wall structure and at both ends of the interface between the deposition layer and the substrate. In order to further characterize the residual stress, the computed stress distributions along three paths: center line of top surface of the substrate perpendicular to the deposition direction (L1), center line of top surface the wall structure along the deposition direction (L2), and center line of top surface of the substrate along the deposition direction (L3), were extracted and compared with the measured values. The findings are depicted in Fig. 10.

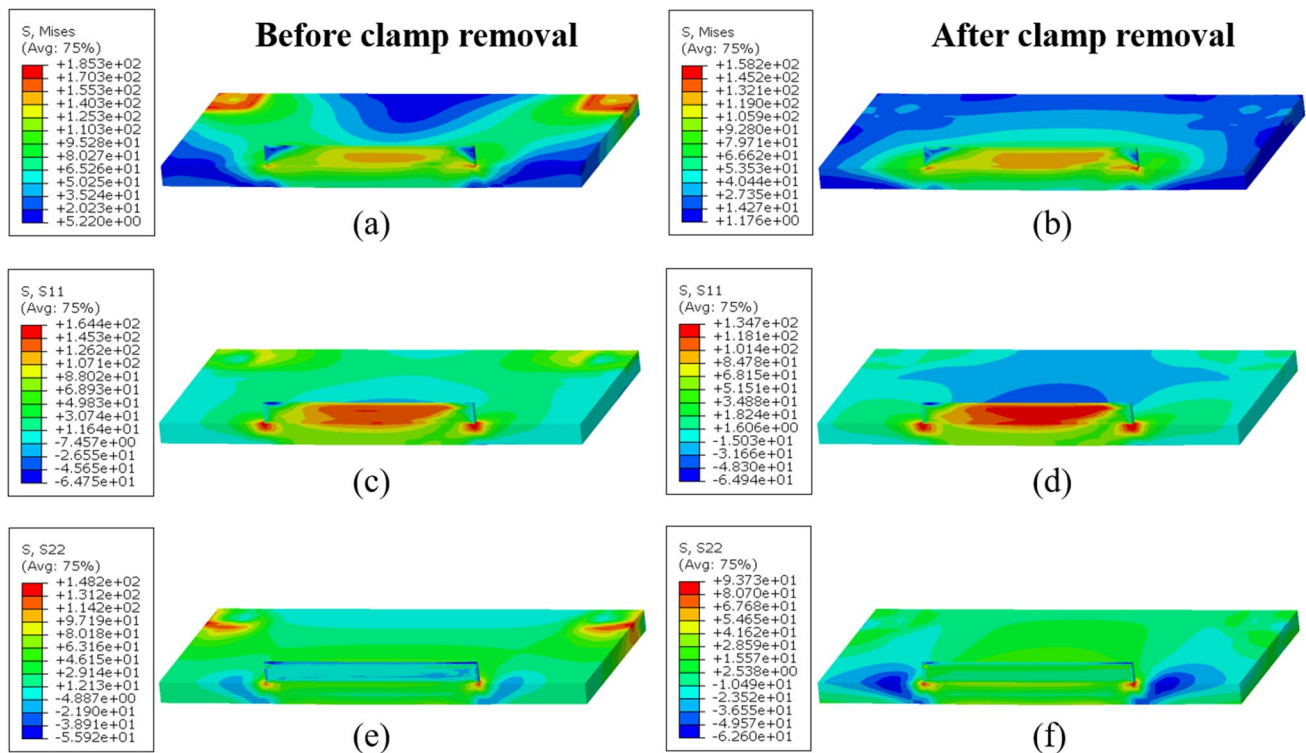


Fig. 9 Stress distributions before and after the clamp removal: **a** and **(b)** the equivalent stress, **c** and **(d)** the longitudinal stress, **e** and **(f)** the transverse stress

Figure 10(a) shows the stress distribution on path L1. It can be observed that the stress value in the internal area of the deposition layer is positive, indicating that the area is subjected to tensile stress. However, the longitudinal stress value in the area away from the deposition layer is negative, indicating that the substrate is subjected to compressive stress. The peak stress occurs at the centerline of the interface between the deposition layer and the substrate. All of the transverse stress value is positive, indicating tensile stress. In the area far from the deposition layer, the transverse stress value is close to zero. Compared to longitudinal stress, the transverse stress value on path L1 is lower. In addition, the measured values of longitudinal stress are relatively close to the calculated values, with errors within 10 MPa, indicating that the calculation model has high accuracy.

In Fig. 10(b), it is apparent that the longitudinal stress on path L2 is negative within about 10 mm from both ends of the deposited wall, and positive in the middle part. It indicates that the top deposition layer is subjected to compressive stress on both ends, and tensile stress in the middle part. The transverse stress along this path is all compressive, and the compressive stress at both ends are higher than the middle part. For comparison, the longitudinal stress at the middle region of the top surface of the wall was measured using XRD. The results were all tensile stress, and agreed

well with the calculated results. The accuracy of the calculation model was verified again in regard to the stress analysis.

In Fig. 10(c), it is clear that the longitudinal stress value is greater than zero, indicating that the top surface of substrate and the interface between deposited wall and substrate are subjected to tensile stress along L3 path. At both ends of the deposition layer, there exist significant stress concentrations. After entering the deposition layer, the stress concentration disappears. The stress is symmetrically distributed, with the longitudinal stress being noticeably greater than the transverse stress.

4.4 Deformation of the substrate

The contour plots of the top and bottom surfaces of the substrate were measured after the EBAM experiment, as shown in Figs. 11(a) and 11 (b). It can be seen that after deposition, four corners the structure are warped upward and the center part is depressed, with a maximum deformation of 0.65 mm. The contour plots of the top and bottom surfaces of the structure were numerically predicted, as shown in Figs. 11(c) and 11 (d). It can be seen that the contour plots are consistent with the experimental measurement results. The deformation trend is the same, and the maximum warping deformation in the thickness direction is 0.71 mm, which is close to the experimental value.

Fig. 10 The distributions of residual stresses in different paths: **a** L1, **b** L2, **c** L3, **d** schematic diagram of different paths

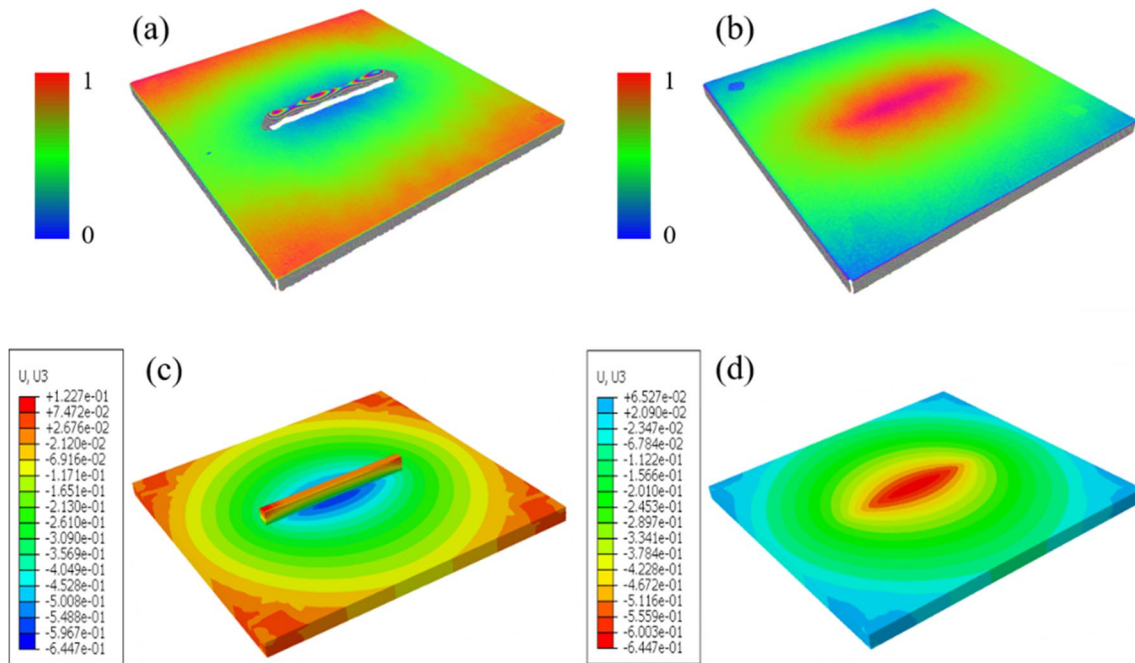
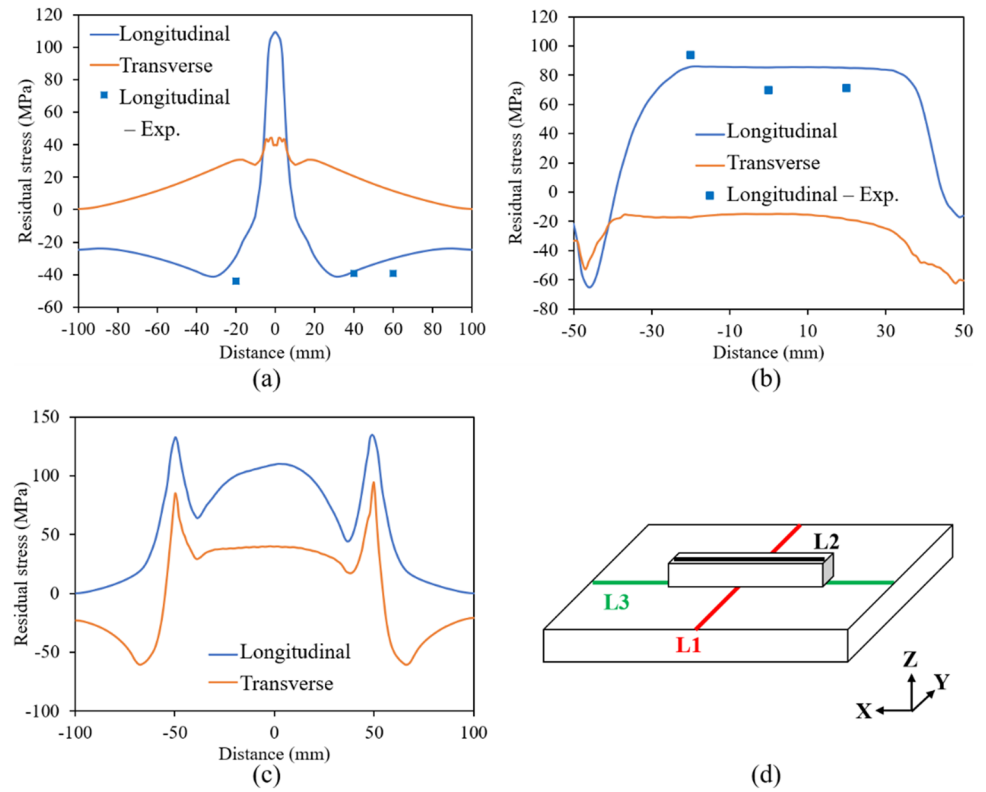


Fig. 11 Deformation of the substrate: measurements of **(a)** top surface and **(b)** bottom surface of the substrate, simulation of **(c)** the top surface and **(d)** bottom surface of the substrate

The deformation along the centerline perpendicular to the deposition direction ($X = 0$) on the bottom surface of the substrate was measured and compared with calculated values, as shown in Fig. 12. It can be found that the calculated value matches the measured value very well.

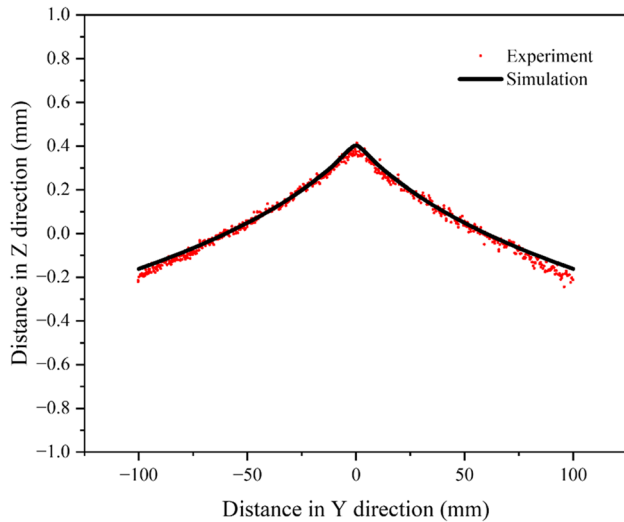


Fig. 12 Deformation along the centerline of the bottom surface of the substrate ($X = 0$)

4.5 The effect of heat input on stress and deformation

The main process parameters involved in the EBAM process include voltage, current, and movement speed, which determine the heat input. Assume the heat input used in the previous sections is Q , and the stress distribution and deformation were calculated for heat inputs of $0.5Q$, $0.75Q$, $1.25Q$, and $1.5Q$, respectively.

The residual stress distributions under different heat inputs are shown in Fig. 13, and the stress is concentrated within the deposition layer. It can be clearly seen that the residual tensile stress increases with the heat input increases. It is widely believed that residual stress is generated due to high cooling rates and large thermal gradients in AM [34, 35]. The increase in heat input causes an increase in cooling rate and temperature gradient, resulting in an increase in residual stress.

Figures 14 and 15 show the deformation results and deformation curves of the bottom surface of the substrate under corresponding heat input, respectively. It can be found that the deformation is positively correlated with the heat input, the larger the heat input, the greater are the deformations. When the heat input is reduced from Q to $0.5Q$, the maximum deformation of the substrate is

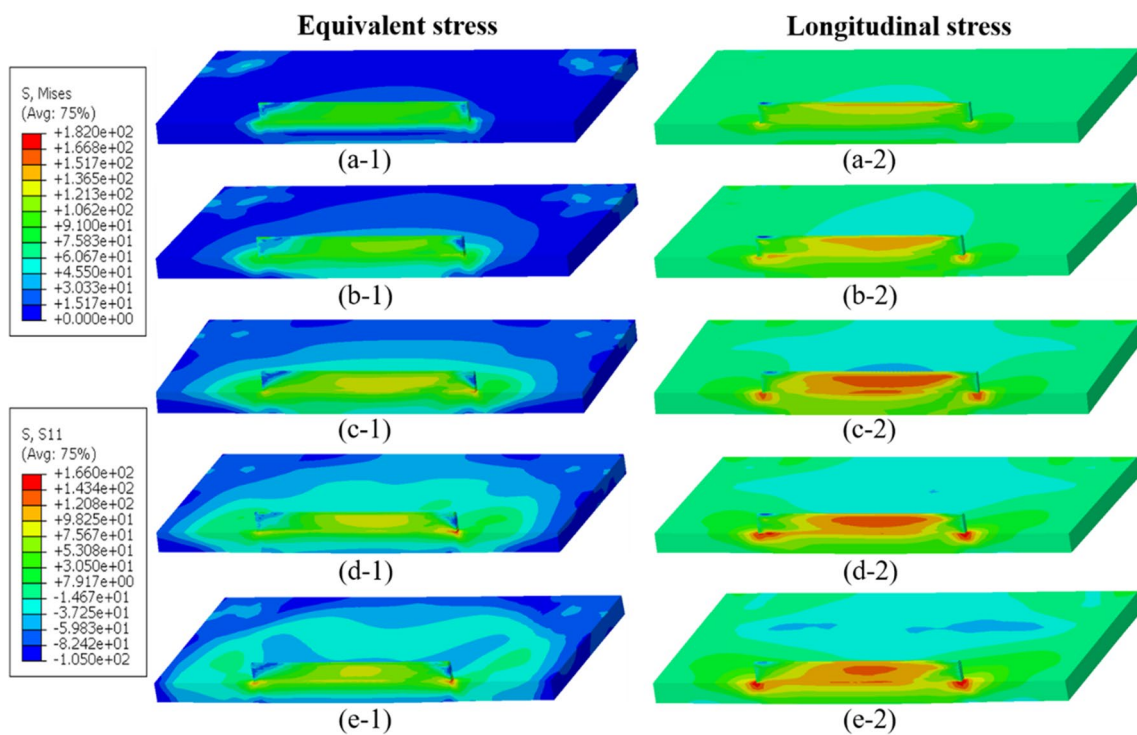


Fig. 13 The effect of heat input on stress distribution: **a** $0.5Q$, **b** $0.75Q$, **c** Q , **d** $1.25Q$, **e** $1.5Q$

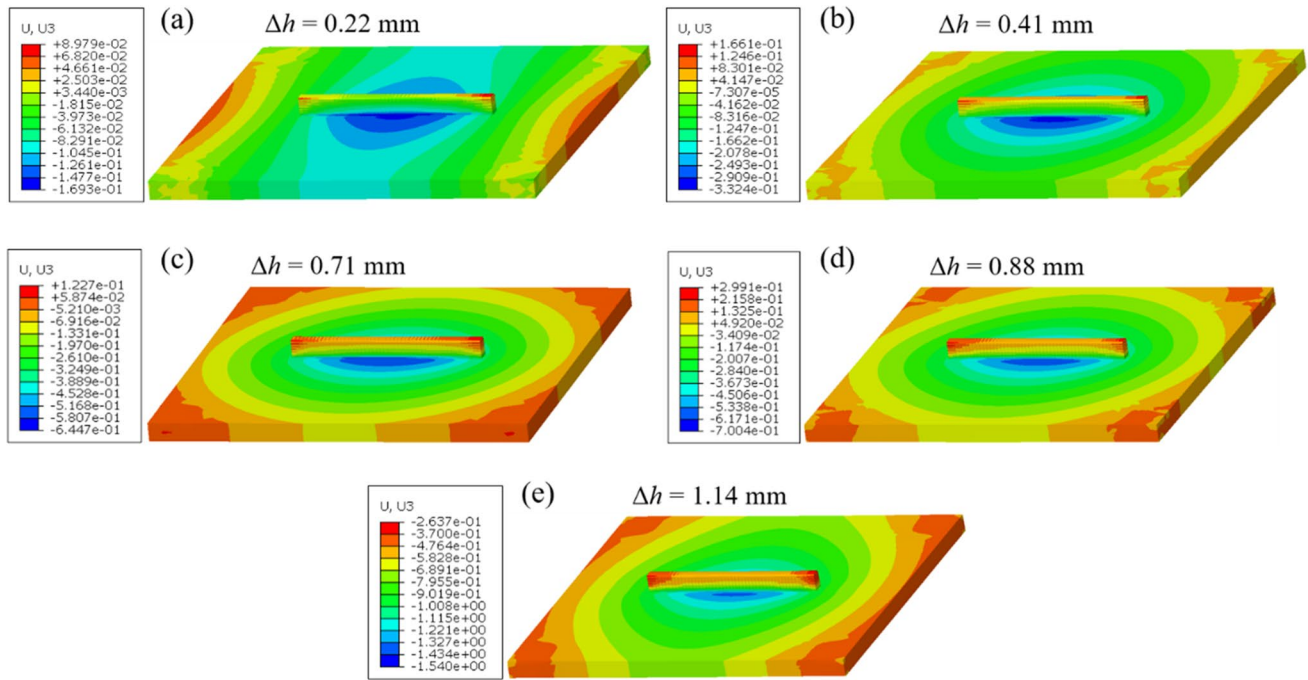


Fig. 14 The effect of heat input on deformation: (a) 0.5Q, (b) 0.75Q, (c) Q, (d) 1.25Q, (e) 1.5Q

reduced from 0.71 mm to 0.22 mm. When the heat input is increased to 1.5Q, the maximum deformation is increased to 1.14 mm. A 69% reduction and a 60.6% increase are resulted, respectively. Therefore, to reduce the deformation of the substrate and control residual stress, heat input can be appropriately reduced.

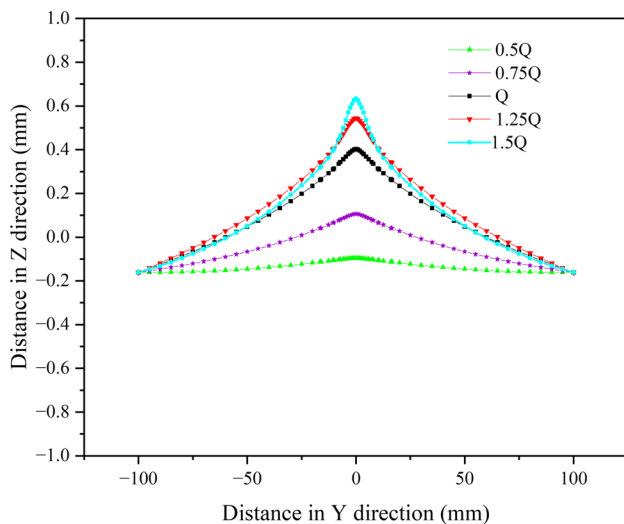


Fig. 15 Deformation along the centerline of the bottom surface of the substrate ($X=0$) for different heat input

5 Conclusions

A three-dimensional transient thermal–mechanical coupled FE model was established to comprehensively simulate the wire-feed EBAM of aluminum alloys for the first time, and the effect of heat input on residual stress and deformation was studied using the model.

- (1) This finite element model has high accuracy in predicting the temperature, stress, and deformation of aluminum alloy wall structures fabricated by wire-feed EBAM.
- (2) Longitudinal residual stress is much higher than transversal residual stress; the high tensile longitudinal residual stress exists mainly at both ends of the interface between the deposit and substrate and in the mid part of the deposited wall.
- (3) With the increase of heat input, the residual tensile stress in the deposition layer increases, and the deformation of the substrate also increases accordingly.

The model established in this work can be a powerful tool to optimize the process parameters in EBAM of aluminum alloy components, which can shorten the process development time and save experimental cost. In addition, it can also be used for controlling residual stress and deformation of EBAM aluminum alloy components.

Acknowledgements The authors would like to thank the editorial department and the reviewers.

Author contributions Conceptualization: Baohua Chang, Dongqi Zhang; methodology: Dong Du, Ze Pu; software: Dongqi Zhang, Yingying Tang; validation: Shuai Xue, Junjie Qi; formal analysis: Dongqi Zhang; investigation: Dongqi Zhang; resources: Yunpeng Lu, Baohua Chang; data curation: Dongqi Zhang; writing-original draft preparation: Dongqi Zhang; writing-review and editing: Baohua Chang; visualization: Baohua Chang; supervision: Dong Du; project administration: Dong Du, Yunpeng Lu; funding acquisition: Baohua Chang.

Funding This work was supported by the Joint Funds of China Academy of Launch Vehicle Technology and University (CALT 2021–24) and the Fund of the State Key Laboratory of Tribology in Advanced Equipment (SKLT2022C20).

Declarations

Conflict of interest The authors declare no conflict of interests.

References

- Herzog D, Seyda V, Wycisk E, Emmelmann C (2016) Additive manufacturing of metals. *Acta Mater* 117:371–392. <https://doi.org/10.1016/j.actamat.2016.07.019>
- Pu Z, Du D, Wang KM, Liu G, Zhang DQ, Wang XB, Chang BH (2021) Microstructure, phase transformation behavior and tensile superelasticity of NiTi shape memory alloys fabricated by the wire-based vacuum additive manufacturing. *Mat Sci Eng A-Struct* 812:141077. <https://doi.org/10.1016/j.msea.2021.141077>
- Zhang DQ, Du D, Pu Z, Xue S, Qi JJ, Chang BH (2023) Interfacial microstructure and stress characteristics of laser-directed energy deposited AA2024 on Ti6Al4V substrate. *Opt Laser Technol* 164:109521. <https://doi.org/10.1016/j.optlastec.2023.109521>
- Liu G, Du D, Wang KM, Pu Z, Zhang DQ, Chang BH (2021) High-temperature oxidation behavior of a directionally solidified superalloy repaired by directed energy deposition. *Corros Sci* 193:109918. <https://doi.org/10.1016/j.corsci.2021.109918>
- Pu Z, Du D, Wang KM, Liu G, Zhang DQ, Zhang HY, Xi R, Wang XB, Chang B (2022) Study on the NiTi shape memory alloys in-situ synthesized by dual-wire-feed electron beam additive manufacturing. *Addit Manuf* 56:102886. <https://doi.org/10.1016/j.addma.2022.102886>
- Wu BT, Pan ZX, Ding DH, Cuiuri D, Li HJ, Xu J, Norrish J (2018) A review of the wire arc additive manufacturing of metals: properties, defects and quality improvement. *J Manuf Process* 35:127–139. <https://doi.org/10.1016/j.jmapro.2018.08.001>
- Zhu ZG, Hu ZH, Seet HL, Liu TT, Liao WH, Ramamurthy U, Nai SML (2023) Recent progress on the additive manufacturing of aluminum alloys and aluminum matrix composites: Microstructure, properties, and applications. *Int J Mach Tool Manu* 190:104047. <https://doi.org/10.1016/j.ijmactools.2023.104047>
- Martin JH, Yahata BD, Hundley JM, Mayer JA, Schaedler TA, Pollock TM (2017) 3D printing of high-strength aluminum alloys. *Nat* 549:365–369. <https://doi.org/10.1038/nature23894>
- Ghasemi A, Fereiduni E, Balbaa M, Jadhav SD, Elbestawi M, Habibi S (2021) Influence of alloying elements on laser powder bed fusion processability of aluminum: A new insight into the oxidation tendency. *Addit Manuf* 46:102145. <https://doi.org/10.1016/j.addma.2021.102145>
- Weingarten C, Buchbinder D, Pirch N, Meiners W, Wissenbach K, Poprawe R (2015) Formation and reduction of hydrogen porosity during selective laser melting of AlSi10Mg. *J Mater Process Technol* 221:112–120. <https://doi.org/10.1016/j.jmatprotec.2015.02.013>
- Bian HK, Aoyagi K, Zhao YF, Maeda C, Mouri T, Chiba A (2020) Microstructure refinement for superior ductility of Al-Si alloy by electron beam melting. *Addit Manuf* 32:100982. <https://doi.org/10.1016/j.addma.2019.100982>
- Kenevisi MS, Lin F (2020) Selective electron beam melting of high strength Al2024 alloy; microstructural characterization and mechanical properties. *J Alloy Compd* 843:155866. <https://doi.org/10.1016/j.jallcom.2020.155866>
- Utyaganova VR, Filippov AV, Shamardin NN, Vorontsov AV, Savchenko NL, Fortuna SV, Gurianov DA, Chumaevskii AV, Rubtsov VE, Tarasov SY (2020) Controlling the porosity using exponential decay heat input regimes during electron beam wire-feed additive manufacturing of Al-Mg alloy. *Int J Adv Manuf Technol* 108:2823–2838. <https://doi.org/10.1007/s00170-020-05539-9>
- Raute J, Biegler M, Rethmeier M (2023) Process Setup and Boundaries of Wire Electron Beam Additive Manufacturing of High-Strength Aluminum Bronze. *Metals* 13:1416. <https://doi.org/10.3390/met13081416>
- Pu Z, Du D, Zhang DQ, Li ZX, Xue S, Xi R, Wang XB, Chang BH (2023) Improvement of tensile superelasticity by aging treatment of NiTi shape memory alloys fabricated by electron beam wire-feed additive manufacturing. *J Mater Sci Technol* 145:185–196. <https://doi.org/10.1016/j.jmst.2022.10.050>
- Li ZX, Cui YN, Chang BH, Liu G, Pu Z, Zhang HY, Liang ZY, Liu CM, Du D (2022) Manipulating molten pool in in-situ additive manufacturing of Ti-22Al-25 Nb through alternating dual-electron beams. *Addit Manuf* 60:103230. <https://doi.org/10.1016/j.addma.2022.103230>
- Liang ZY, Chang BH, Zhang HY, Li ZX, Peng GD, Du D, Chang SH, Wang L (2022) Electric current evaluation for process monitoring in electron beam directed energy deposition. *Int J Mach Tool Manu* 176:103883. <https://doi.org/10.1016/j.ijmactools.2022.103883>
- Prabhakar P, Sames WJ, Dehoff R, Babu SS (2015) Computational modeling of residual stress formation during the electron beam melting process for Inconel 718. *Addit Manuf* 7:83–91. <https://doi.org/10.1016/j.addma.2015.03.003>
- Simson T, Emmel A, Dwars A, Böhm J (2017) Residual stress measurements on AISI 316L samples manufactured by selective laser melting. *Addit Manuf* 17:183–189. <https://doi.org/10.1016/j.addma.2017.07.007>
- Zhang WY, Guo D, Wang L, Davies CM, Mirihanage W, Tong MM, Harrison NM (2023) X-ray diffraction measurements and computational prediction of residual stress mitigation scanning strategies in powder bed fusion additive manufacturing. *Addit Manuf* 61:103275. <https://doi.org/10.1016/j.addma.2022.103275>
- Swain D, Sharma A, Selvan SK, Thomas BP, Govind PJ (2019) Residual stress measurement on 3-D printed blocks of Ti-6Al-4V using incremental hole drilling technique. *Procedia Struct Integr* 14:337–344. <https://doi.org/10.1016/j.prostr.2019.05.042>
- Sandmann P, Keller S, Kashaev N, Ghouse S, Hooper PA, Klusemann B, Davies CM (2022) Influence of laser shock peening on the residual stresses in additively manufactured 316L by Laser Powder Bed Fusion: A combined experimental–numerical study. *Addit Manuf* 60:103204. <https://doi.org/10.1016/j.addma.2022.103204>
- Shen C, Ma Y, Reid M, Pan ZX, Hua XM, Cuiuri D, Paradowska A, Wang L, Li HJ (2022) Neutron diffraction residual stress determinations in titanium aluminide component fabricated using the twin wire-arc additive manufacturing. *J Manuf Process* 74:141–150. <https://doi.org/10.1016/j.jmapro.2021.12.009>

24. Nycz A, Lee Y, Noakes M, Ankit D, Masuo C, Simunovic S, Bunn J, Love L, Oancea V, Payzant A, Fancher CM (2021) Effective residual stress prediction validated with neutron diffraction method for metal large-scale additive manufacturing. *Mater Des* 205:109751. <https://doi.org/10.1016/j.matdes.2021.109751>
25. Sun JM, Hensel J, Köhler M, Dilger K (2021) Residual stress in wire and arc additively manufactured aluminum components. *J Manuf Process* 65:97–111. <https://doi.org/10.1016/j.jmapro.2021.02.021>
26. Zhao ZY, Wang JB, Du WB, Bai PK, Wu XY (2023) Numerical simulation and experimental study of the 7075 aluminum alloy during selective laser melting. *Opt Laser Technol* 167:109814. <https://doi.org/10.1016/j.optlastec.2023.109814>
27. Caiazzo F, Alfieri V, Bolelli G (2021) Residual stress in laser-based directed energy deposition of aluminum alloy 2024: simulation and validation. *Int J Adv Manuf Technol* 118:1197–1211. <https://doi.org/10.1007/s00170-021-07988-2>
28. Vastola G, Zhang G, Pei QX, Zhang YW (2016) Controlling of residual stress in additive manufacturing of Ti6Al4V by finite element modeling. *Addit Manuf* 12:231–239. <https://doi.org/10.1016/j.addma.2016.05.010>
29. Chen Z, Ye H, Xu HY (2018) Distortion control in a wire-fed electron-beam thin-walled Ti-6Al-4V freeform. *J Mater Process Technol* 258:286–295. <https://doi.org/10.1016/j.jmatprotec.2018.04.008>
30. Cao J, Gharghoury MA, Nash P (2016) Finite-element analysis and experimental validation of thermal residual stress and distortion in electron beam additive manufactured Ti-6Al-4V build plates. *J Mater Process Technol* 237:409–419. <https://doi.org/10.1016/j.jmatprotec.2016.06.032>
31. Raghavan N, Dehoff R, Pannala S, Simunovic S, Kirka M, Turner J, Carlson N, Babu SS (2016) Numerical modeling of heat-transfer and the influence of process parameters on tailoring the grain morphology of IN718 in electron beam additive manufacturing. *Acta Mater* 112:303–314. <https://doi.org/10.1016/j.actamat.2016.03.063>
32. Denlinger ER, Heigel JC, Michaleris P (2015) Residual stress and distortion modeling of electron beam direct manufacturing Ti-6Al-4V. *P I Mech Eng B J Eng* 229:1803–1813. <https://doi.org/10.1177/0954405414539494>
33. Chen GQ, Shu X, Liu JP, Zhang BG, Feng JC (2020) A new method for distortion calculations in additive manufacturing: contact analysis between a workpiece and clamps. *Int J Mech Sci* 171:105362. <https://doi.org/10.1016/j.ijmecsci.2019.105362>
34. Kruth JP, Deckers J, Yasa E, Wauthlé R (2012) Assessing and comparing influencing factors of residual stresses in selective laser melting using a novel analysis method. *P I Mech Eng B J Eng* 226:980–991. <https://doi.org/10.1177/0954405412437085>
35. Zhao L, Macías JGS, Dolimont A, Simar A, Rivière-Lorphèvre E (2020) Comparison of residual stresses obtained by the crack compliance method for parts produced by different metal additive manufacturing techniques and after friction stir processing. *Addit Manuf* 36:101499. <https://doi.org/10.1016/j.addma.2020.101499>

Publisher's Note Springer Nature remains neutral with regard to jurisdictional claims in published maps and institutional affiliations.

Springer Nature or its licensor (e.g. a society or other partner) holds exclusive rights to this article under a publishing agreement with the author(s) or other rightsholder(s); author self-archiving of the accepted manuscript version of this article is solely governed by the terms of such publishing agreement and applicable law.